Active Area Dependence of Optoelectronic Characteristics of Perovskite LEDs

*Iakov Goldberg[1,2], Weiming Qiu[1,3] *, Karim Elkhouly[1,2], Nirav Annavarapu[1,2], Ankit Nalin Mehta[1], Cedric Rolin[1], Tung-Huei Ke[1], Robert Gehlhaar[1], Jan Genoe[1,2], and Paul Heremans[1,2] **

[1] IMEC, Kapeldreef 75, Leuven 3001, Belgium.

[2] ESAT, KU Leuven, Kasteelpark Arenberg, Leuven 3001, Belgium.

[3] Department of Chemistry, KU Leuven, Celestijnenlaan 200F, 3001 Leuven, Belgium.

KEYWORDS: metal halide perovskite, perovskite light-emitting diode, operational stability, perovskite laser, high current density, Joule heating

ABSTRACT: Organometallic halide perovskites are non-epitaxial low-temperature semiconductors that show great promise in light-emission applications due to their favorable optoelectronic properties. Though high external quantum efficiencies exceeding 20 % have been shown for perovskite LEDs, this is usually achieved at low current densities, and hence corresponds to low brightness. To reach high brightness, it is important to make strides in stability and quantum efficiency at high current density. In this work, we scale the active area of methylammonium lead iodide perovskite LEDs from 1000 μm in diameter down to tens of microns dimensions, relevant for emissive displays and laser devices that require high brightness. We systematically examine active-area-dependent perovskite

LED performance from mA·cm^{-2} up to kA·cm^{-2} current density regimes by means of quasi-DC, DC, and sub-μs pulsed driving. For perovskite LEDs with diameters of 50 μm on glass substrates, we achieve T_{50} stability above 10 h under continuous operation at 500 mA·cm^{-2} and above 5 h at 1000 mA·cm^{-2}, respectively. By using short electrical pulses, we significantly reduce the amount of dissipated thermal energy and show that this leads to reliable electrical operation up to 5 kA·cm^{-2} for such small perovskite LEDs fabricated on sapphire substrates.

1. Introduction

Organometallic halide perovskites have recently arisen as an outstanding class of functional materials for next-generation solar cells,[1,2] photodetectors,[3,4] displays,[5,6] and lasers.[7,8] Specifically, perovskite light-emitting diodes (PeLEDs) have seen a rapid advancement in the past few years. Continuous development of highly emissive perovskite materials and novel material combinations has pushed perovskites ever closer to the coverage of the entire Rec. 2020 color space standard for wide-gamut displays. Most of these PeLEDs exploit low-dimensional perovskite active layers either in the form of nanocrystals or quasi 2D/3D nanostructures that provide good carrier confinement.[9,10] As a result, external quantum efficiency (EQE) of the most efficient PeLEDs has surpassed 20 % and is nearly on par with that of the state-of-the-art organic and quantum-dot LEDs.[11,12] Furthermore, optically-pumped perovskite lasers with low lasing threshold were reported,[13,14] directing attention towards an electrically-pumped laser.

The realization of the electrically-driven perovskite laser diode, which has strong commercialization potential, requires a significant light generation efficiency at hundreds or thousands of A·cm^{-2} to exceed a lasing threshold condition. However, the low thermal conductivity of organic-inorganic lead halide perovskites makes thermal management a critical factor in the feasibility of high brightness and

lasing applications.[15] Shrinking the device area would allow to achieve a small pumping volume, such that the lasing-level current density injection could be realized at a low absolute current passing through the device. To date, although small-area PeLEDs with high-current density injection up to several kA·cm^{-2} have been demonstrated,[16,17] a systematic study for a deeper understanding of the active-area-dependent PeLED performance and scaling implications across multiple current densities is still lacking.

In this work, we investigate the active-area-dependent performance of bottom-emitting PeLEDs with sizes ranging from $7.85 \cdot 10^{-3}$ cm^2 down to $1.96 \cdot 10^{-5}$ cm^2 on glass and sapphire substrates under quasi-DC bias, continuous bias, and pulsed driving operation. For the chosen device area, we show that low current density operation (below 1000 mA·cm^{-2}) is not affected by the chosen device active area but is rather prone to device-to-device variation. In contrast, in the high current density region, EQE roll-off depends on the chosen biasing scheme and is highly active-area-dependent. In this regime, both EQE roll-off and device stability improve with the reduced device area due to the mitigation of Joule heating. Using a PeLED with a diameter of 50 μm fabricated on sapphire substrate, we achieve a high quasi-DC radiance of 2059 W·m^{-2}·sr^{-1}, half-life time above 10 h under continuous operation at 500 mA·cm^{-2}, and a high EQE × J product value of 6.7 A·cm^{-2} at a pulsed current density of 4.17 kA·cm^{-2}. This work reveals the correlation between device optoelectronic performance and active area and provides a better understanding of PeLED behavior under different operation modes.

2. Results and Discussion

2.1. Structural characterization of scaled devices. The device area of our PeLEDs is defined via a lithographically patterned circular opening in an insulating SiN layer deposited on top of the indium tin oxide (ITO) electrode. We complete the PeLED architecture by a sequential spin-coating of functional layers and the evaporation of Al electrode. **Figure 1 a** shows the PeLED structure and its

active area definition. The fabrication details are elaborated in the **Experimental Section** and **Supplementary Figure S1**. We achieve devices with well-controlled active areas, ranging from $7.85 \cdot 10^{-3}$ cm^2 (for ⌀1000 μm circular opening) to $1.96 \cdot 10^{-5}$ cm^2 (for ⌀50 μm) (**Supplementary Table S2)**. The PeLED architecture is based on methylammonium lead iodide ($MAPbI_3$) emission layer sandwiched between a poly-TPD hole transport layer and a PCBM/ZnMgO electron transport bilayer. ITO and Al are used as hole- and electron-injection ohmic electrodes, respectively. By adding a large organic cation PMAI to the perovskite precursor, we obtain a smooth, passivated nanocrystalline $MAPbI_3$:PMAI active layer following the approach from the previous work.[18] Here, poly-TPD, PCBM, ZnMgO, and PMAI respectively refer to poly-[N,N′-bis(4-butylphenyl)-N,N′-bis(phenyl)-benzidine]; 6,6'-phenyl-C_{61}-butyric acid methyl ester; magnesium-doped zinc oxide; and benzylammonium iodide. We have previously demonstrated high operational stability for the same stack,[19] which sparked our interest to study equivalent devices with miniaturized areas at high current densities.

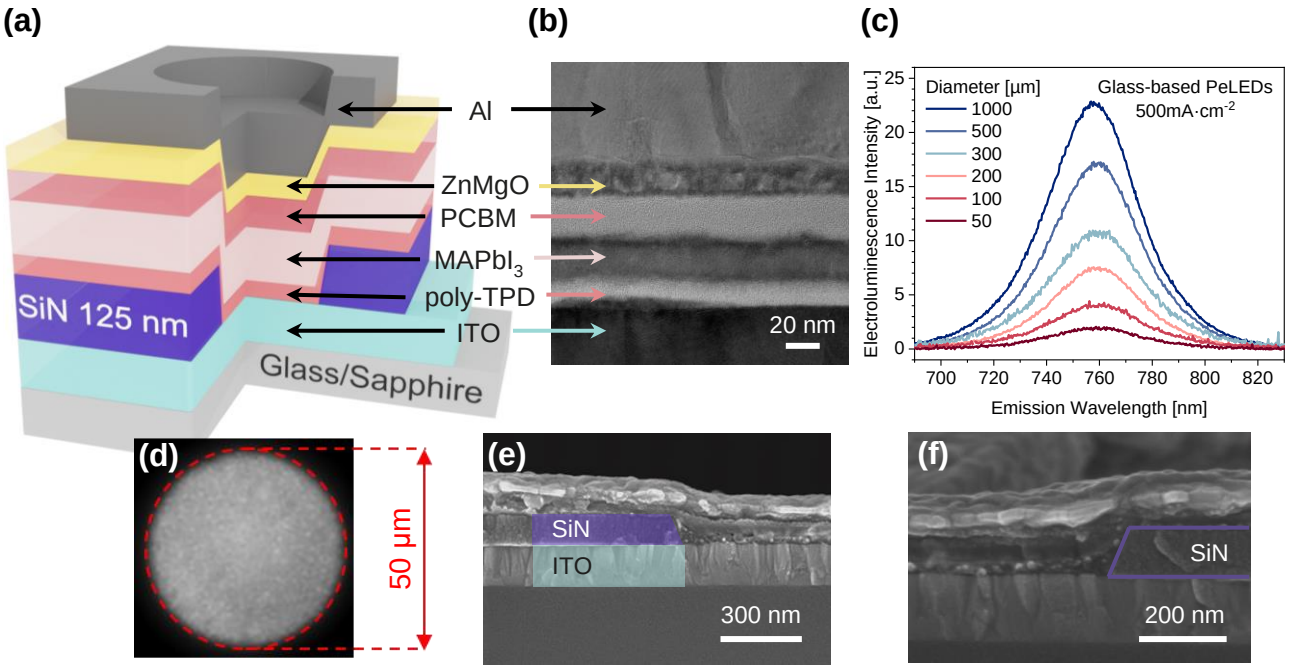

Figure 1. Structural and geometrical characteristics of the fabricated circular PeLEDs. (a) Schematics of bottom-emitting PeLEDs. SiN pixel definition layer (purple) is 125 nm thick. The dimensions are not to scale. (b) Cross-sectional HR-TEM image in the bulk of the pristine 1000 μm device. (c) Electroluminescence spectra recorded with variable integration time at a constant current density of 500 mA·cm^{-2} for PeLEDs fabricated atop a glass substrate. At this current density, the emission is centered around 757 nm. (d) Spatial electroluminescence image for 50 μm glass-based PeLED driven at a current density of 500 mA·cm^{-2}. Red border marks the edges of the device. (e) Cross-sectional SEM analysis of pristine PeLED. (f) Zoomed-in SEM picture.

Cross-sectional high-resolution transmission electron microscopy (HR-TEM) image (**Figure 1 b**) of fabricated PeLEDs shows clear interfaces between layers and confirms the targeted layers' thicknesses in the bulk of the investigated devices. Fabricated PeLEDs show no significant optical cavity variation, as was supported by measuring electroluminescence spectra at 500 mA·cm^{-2} (**Figure 1 c**). In our analysis, we neglect the variation of light extraction efficiency due to the possible scattering off the dielectric sidewalls or other cavity effects. These effects are not observable even for smallest devices

used in this work (**Figure 1 d**). Moreover, electroluminescence intensity remains largely spatially uniform across a large current density range for variable-area PeLEDs (**Supplementary Figure S3)**. **Figures 1 e** and **f** depict scanning electron microscopy (SEM) images of the device cross-section recorded at different magnifications. The chosen solution deposition method of thin functional layers might impose a great challenge to grow conformal layers next to SiN edge that presents a step height of 125 nm with a positive slope angle around 70°. We observe that the total thickness of the device in the vicinity of SiN edge is often different from that of the bulk. However, layer uniformity is reached within 300 nm from the edge (**Figures 1 e** and **1 f**), making this effect insignificant to our devices which have a minimum diameter of 50 μm. We anticipate edge effects to be more prominent for the more scaled and anisotropic architectures because of an increased edge-to-surface ratio. Similar detrimental implications were reported when stacking a much thicker perovskite functional layer on top of a substrate with a considerable roughness during the fabrication of tandem solar cells.[20,21]

2.2. Operation under quasi-DC bias. We begin by evaluating the device area dependence of the *J-V*, EQE-*J*, and Radiance-*J* characteristics for the glass-based PeLEDs measured in the quasi-DC regime. In this biasing scheme, each data point is acquired by applying 20 ms pulses with 20 s idle time. The chosen idle time is sufficiently long to allow for complete thermal dissipation in-between consecutive pulses, which considerably extends device operation and improves data interpretation.[22] For all devices, *J-V* curves in **Figure 2 a** align in the moderate voltage bias regime (between turn-on at ≈ 0.9 V and 2 V), while showing a marked variation in the ohmic (below 0.9 V) and high injection regimes (above 2 V). The lower limit of absolute current is likely set by a ≈ 1.3 GOhm current leakage path through a SiN parasitic capacitor and/or possibly through the patterned SiN edge. The area of the SiN parasitic capacitor is defined by the overlapping top and bottom electrodes and is independent of the device electrical area (**Supplementary Figure S4**). Current density reduction across larger devices

at the same voltage bias is caused by a greater series resistance voltage loss for bigger devices for the same current density (but for a higher absolute current).

Comparing the performance of the scaled PeLEDs on glass substrates, the measurement of more than a hundred variable-sized devices resulted in a mean EQE_{MAX} of 5.6 % with outliers reaching above 9 % (**Supplementary Figure S5**). The smallest 50 μm PeLEDs show the most significant device-to-device variation, with a standard deviation more than twofold broader than for 1000 μm devices, due to their increased vulnerability to non-radiative defects. The size effects on the PeLED electroluminescence intensity and roll-off are presented in **Figure 2 b**. Below 1000 $mA \cdot cm^{-2}$, EQE-*J* curves show no direct dependence on the active area. It is also the region where most of the investigated devices reach their maximum EQE values. For PeLEDs on glass substrates at current densities beyond EQE_{MAX}, smaller devices yield higher EQEs in comparison to larger PeLEDs, irrespective of EQE_{MAX} differences. Device active area becomes of paramount importance for PeLED operation in high-current density regime, where Joule heat generated during the 20 ms pulses exerts adverse impact on light output. Recorded radiances are significantly deteriorated for the larger glass-based devices past 2-3 $A \cdot cm^{-2}$ (**Figure 2 c)**. It is clearly seen that the greatest radiances are delivered by the smallest emitting areas, which are also capable to withstand an application of current densities above 15 $A \cdot cm^{-2}$ without irreversible degradation. We observe that the onset of device irreversible degradation is closely linked to the decay in radiance curves, without notable differences in *J*-*V* output (**Supplementary Figure S6**).

A highly thermally conductive substrate such as sapphire (thermal conductivity of 25 $W \cdot m^{-1} \cdot K^{-1}$) is used instead of glass (1.4 $W \cdot m^{-1} \cdot K^{-1}$) in conjunction with small effective areas to provide an efficient pathway for heat dissipation.[23] Consequently, we evaluate similar bottom-emitting PeLEDs on sapphire substrates in the quasi-DC regime to prove that the active-area-dependent roll-off and

irreversible degradation behavior are related to Joule self-heating. The *J-V* plots of the sapphire-based PeLEDs in **Figure 2 d** are comparable to their glass counterparts, except for the need of higher voltage to reach current densities above 10 $A \cdot cm^{-2}$. This is caused by the use of in-house ITO thin films with a higher sheet resistance of around 40 $\Omega \cdot sq^{-1}$. The EQE-*J* plots in **Figure 2 e** and Radiance-*J* plots in **Figure 2 f** clearly reveal the differences between the devices made on sapphire and glass substrates. The PeLEDs atop sapphire show similar EQE roll-off behavior for all investigated sizes, unlike the devices on glass substrates that result in strong active-area-dependent operation. Moreover, no PeLEDs on sapphire show a sign of irreversible degradation within the measurement range, with overall higher radiances than for glass-based devices above 10 $A \cdot cm^{-2}$ even for the smallest devices. On the one hand, these results indicate that a more severe EQE roll-off and lower PeLED stability on glass substrates are indeed related to Joule heating, and such effects are strongly mitigated by the higher thermal conductivity of sapphire substrates. On the other hand, the above results also imply that the device downscaling alone is not sufficient to achieve the optimal device performance at a high current density injection. It is therefore essential to combine miniaturized active areas with the use of highly thermally conductive substrates. Indeed, for the PeLEDs with 50 μm diameter, we achieve a remarkably higher quasi-DC radiance of 2059 $W \cdot m^{-2} \cdot sr^{-1}$ on the sapphire substrate than that of 1418 $W \cdot m^{-2} \cdot sr^{-1}$ on the glass substrate (**Supplementary Figure S7**).

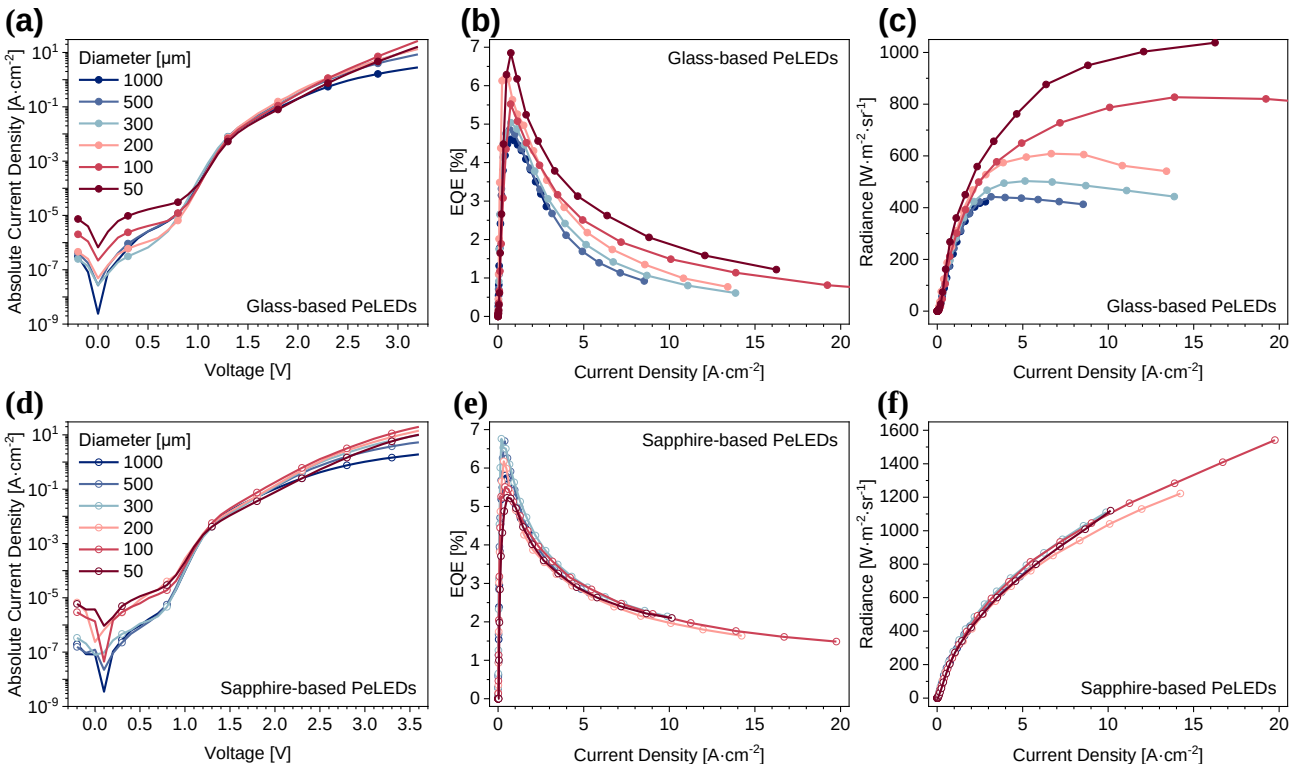

Figure 2. Active-area-dependent optoelectronic characteristics of glass-based (top row) and sapphire-based (bottom row) $MAPbI_3$ PeLEDs recorded at room temperature in a quasi-DC regime. (a) and (d) *J*-*V* characteristics. (b) and (e) EQE-*J*. (c) and (f) Radiance-*J* curves. The presented dataset is extracted from the two samples, fabricated on a corresponding transparent substrate. The auxiliary plots are to be found in **Supplementary Figure S4**.

2.3. Operation under continuous bias. In the following, we evaluate glass-based devices with variable sizes utilizing continuous *J*-*V* scans, as is commonly adopted in the literature.[24,25] Compared to the above-reported quasi-DC scans, a continuous bias without idle time may lead to heat accumulation, resulting in the more significant active-area-dependent effects.

Figure 3 shows Radiance-*J*-*V* and EQE-*J* curves of the exemplary 1000 µm and 300 µm glass-based devices, measured in forward and reverse directions at different scan rates and current density ranges. In our previous work, we showed that these scan parameters exert a profound influence on the PeLED

optoelectronic characteristics.[22] Performance hysteresis at slow scan rates and large scan ranges is mainly linked to the Joule heat accumulation and irreversible degradation occurring during continuous measurements. From **Figures 3 a** and **3 b** it follows that the 1000 μm device shows almost no hysteresis when the *J-V* scan is limited to 2.5 V or 1.8 $A \cdot cm^{-2}$. However, severe device hysteresis can be observed at all scan rates when biased up to 4.5 $A \cdot cm^{-2}$ (**Figures 3 c** and **3 d**). On the contrary, under similar *J-V* operation up to ≈ 4 $A \cdot cm^{-2}$, the 300 μm device shows no appreciable device hysteresis (**Figures 3 e** and **3 f**). Instead, for this device, electroluminescence hysteresis appears when measured up to a much higher current density of 10 $A \cdot cm^{-2}$ and only at scan rates slower than 0.2 $V \cdot s^{-1}$. The reported heat accumulation is fully reversible as EQE-*J* curves continue to align in the forward sweep in the sequential scans. Therefore, the device downscaling helps to mitigate electroluminescence hysteresis under continuous *J-V* scans up to a certain current density. Similar to the quasi-DC operation, the smaller device active area also significantly improves EQE roll-off behavior due to the decreased Joule heating. The elimination of light output hysteresis indicates the negligible role of Joule heating on EQE roll-off. This enables us to decouple the role of Joule heating from other effects such as charge balance,[26] non-radiative defects,[27] etc., which is necessary for the interpretation of EQE roll-off behavior.

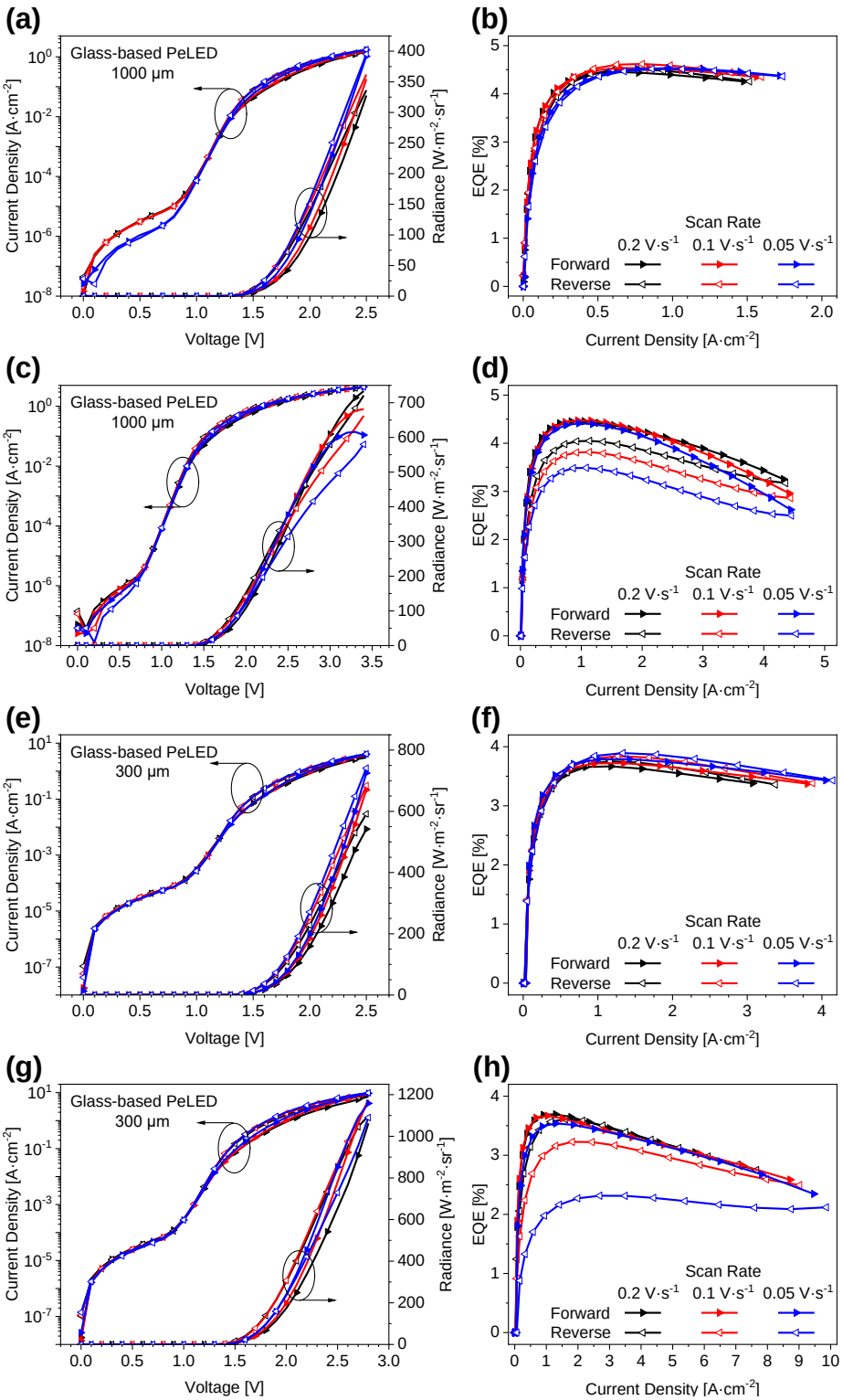

Figure 3. Radiance-*J*-*V* and EQE-*J* characteristics of the exemplary glass-based PeLEDs, sequentially measured in a continuous DC mode with decreasing voltage scan rates of 0.2 $V \cdot s^{-1}$, 0.1 $V \cdot s^{-1}$, and 0.05 $V \cdot s^{-1}$. Measurements (a)-(d) represent a larger 1000 μm device, whereas (e)-(h)

refer to a smaller 300 μm device. 1000 μm PeLED is measured three times at decreasing scan rates up to 2.5 V and then immediately back to 0 V, (a)-(b). Shortly after, the three forward and reverse measurements limited to 3.4 V are acquired, (c)-(d). Similarly, 300 μm PeLED is measured three times at decreasing scan rates up to 2.5 V and then back to 0 V, (e)-(f), followed by three 0 V – 2.8 V – 0 V (g)-(h) scans.

We then further investigate active-area-dependent PeLED performance under a continuous constant current bias, i.e., PeLED operational stability. Operational stability remains an as-yet unsolved challenge for PeLEDs.[28] It is well-acknowledged that elevated perovskite temperatures accelerate first-order degradation mechanisms such as ion migration, electrochemical reactions, or interfacial reactions, and thus limit PeLED lifetime.[29,30]

Figure 4 a shows the normalized electroluminescence intensity as a function of time for the glass-based devices biased at a constant current density of 500 $mA \cdot cm^{-2}$. Interestingly, only the largest device with a diameter of 1000 μm suffers from an accelerated irreversible degradation and departs from the equilibrium operation after around 200 min. This instability is preceded by an increase in voltage and injected power (**Supplementary Figure S8**). In contrast, smaller glass-based devices can sufficiently dissipate Joule heat due to the lower thermal power input. Throughout the prolonged operation, these smaller PeLEDs maintain thermal equilibrium.

The underlined effect of heat accumulation on the PeLED stability is supported by the following two facts. First, when biasing the devices at a higher current density of 1000 $mA \cdot cm^{-2}$ (**Figure 4 b**), we observe that the difference between the 1000 μm device and the smaller devices becomes more pronounced due to the increased input thermal power and a limited heat dissipation capability of the glass substrate. Second, sapphire-based devices do not show significant discrepancies in degradation

speed when biased at 500 $mA \cdot cm^{-2}$, as sapphire substrate prevents heat accumulation in the perovskite junction for all the studied areas (**Figure 4 c)**.

It is also noteworthy that the largest device in this study is significantly smaller than most of PeLEDs reported in literature. Those larger PeLEDs should show more dramatic active-area-dependent effects. Moreover, since there is no accepted device active area standard across the PeLED community, it becomes important to account for differences in PeLED area when comparing operational stability results from different research groups. Furthermore, it is also clear that device area downscaling is not sufficient to eliminate root causes of PeLED operational instability. Both T_{90} and T_{50} decrease almost twofold even for the smallest glass-based samples when operated at 1000 $mA \cdot cm^{-2}$ instead of 500 $mA \cdot cm^{-2}$. Even in the absence of accumulated heat effects, severe device degradation is triggered by mechanisms such as ion migration,[31] assisted by a strong electric field across a thin device stack. In case of our stable PeLED architecture, we demonstrate T_{50} stability above 10 h under continuous operation at 500 $mA \cdot cm^{-2}$ and 5 h at 1000 $mA \cdot cm^{-2}$, respectively. In addition, the choice of single-component perovskite composition allows preserving device spectral stability (**Supplementary Figure S9**).

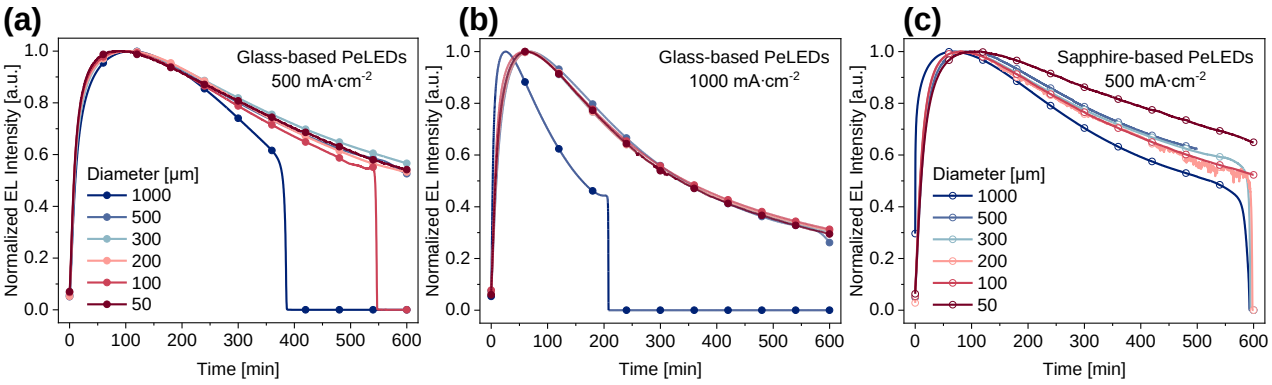

Figure 4. Constant-current lifetime electroluminescence (EL) measurements recorded for variable PeLED active areas at (a) 500 mA·cm^{-2} and (b) 1000 mA·cm^{-2} for glass-based devices and at (c) 500 mA·cm^{-2} for sapphire-based devices.

2.4. Operation under sub-μs pulsing. To investigate the active-area-dependent device performance at even higher current densities, up to several kA·cm^{-2}, relevant for injection-lasing,[32,33] we use sapphire-based devices similar to those of **Figures 2 d-f**. Herein, the scaled devices are biased in μs/ns pulsed driving mode with a low frequency of 10 Hz (**Figure 5 a**). This minimizes Joule heating effects and allows probing the devices reliably at current densities up to 5 kA·cm^{-2}, while avoiding the device degradation due to intense electrical excitation. The pulse width is adjusted between 2000 ns and 250 ns, where it is systematically reduced for higher current densities. It is important to note that each pulsing data point is captured after 50 pulses, during which the device performance remains highly reproducible. In these experiments, the injected current density became quickly dominated by the ITO series resistance at higher voltage biases, thus allowing the smaller devices to reach a higher current density operation at a lower peak voltage. The larger devices could reach at least 80 A·cm^{-2}, and the smaller ones - even up to 5 kA·cm^{-2}.

Formerly, Kim et al. showed the importance of pulse train time-averaged history and mobile ions distribution on the PeLED operation, where adding a background bias (V_{bias}) enhances the device performance when pulsed in the μs/ns range.[32] This effect is particularly important in the low current density range. For our PeLEDs, we have used a fixed V_{bias} = 1.9 V across all measurements. This allows matching EQE values obtained in the quasi-DC mode (dots) with that of the sub-μs pulsed mode (lines), as shown in **Figure 5 b**. In the current density regime above 20 A·cm^{-2}, all miniaturized sapphire-based devices show a monotonic decrease in EQE, resulting in the EQE values of 0.33 % at 1 kA·cm^{-2} and 0.13 % at 5 kA·cm^{-2}. By investigating the light signal at different current densities ranging from 28 A·cm^{-2} to 5.23 kA·cm^{-2} for a 50 μm device, we find that the effect of Joule heating is largely mitigated using short electrical pulses and only becomes apparent at current densities above 900 A·cm^{-2} for the chosen pulse widths. This is reflected in the negative slope of the photodetector signal (**Figure 5 c**).[16,32] For even higher current densities, the heating effect becomes more severe such that the radiance at 5.23 kA·cm^{-2} is lower than that at 4.17 kA·cm^{-2}, where a maximum brightness of ≈ 35 kW·m^{-2}·sr^{-1} is achieved. Electroluminescence pulse shape shows no alteration in-between repetitive application of these intermittent current density pulses, as heat has enough time to diffuse away from the perovskite junction region due to the low duty cycle of applied pulses. In the meantime, we observe that the current density pulse shape does not reflect the effect of Joule heating during the device operation (**Supplementary Figure S10**). **Figure 5 d** shows that the EQE × J product of our devices reaches the maximum value of 6.7 A·cm^{-2} at a current density of 4.17 kA·cm^{-2}, after which it starts to decay due to the dominant effect of Joule heating. It is estimated that observing amplified spontaneous emission would require the EQE × J product of 33-95 A·cm^{-2}.[16,17] Our result implies that the goal of achieving an electrically-pumped perovskite laser might be within reach if the device performance at high current densities is further improved. It can also be seen that EQE × J product

curves of the investigated variable-sized devices follow the same trend, indicating negligible active-area-dependent effects when pulsed with proper pulse width and duty cycle adjustments.

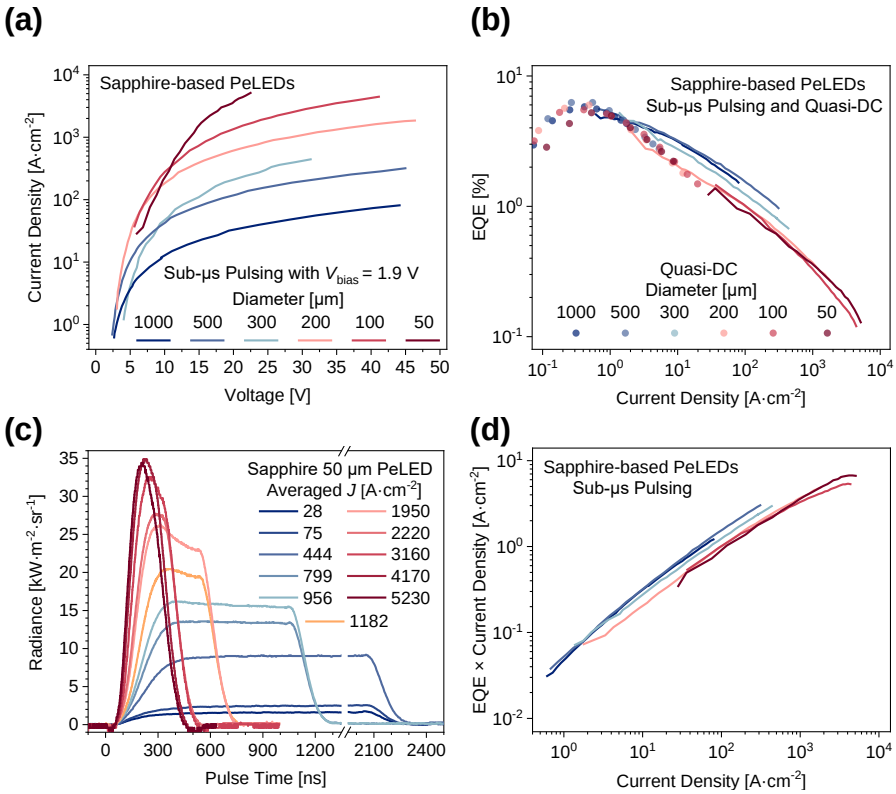

Figure 5. Sapphire-based PeLED operation under pulsed sub-µs driving. V_{bias} is fixed at 1.9 V. (a) Pulsed *J*-*V* characteristics. (b) Pulsed EQE-*J* characteristics. Quasi-DC results are overlayed for comparison (translucent dots). (c) Radiance pulsed output for 50 µm sapphire-based device. The pulse times are 2000 ns, 1000 ns, 500 ns, 300 ns, and 250 ns. (d) EQE × *J* product with a maximum of 6.7 A·cm^{-2}, achieved at a current density of 4.17 kA·cm^{-2} for the smallest 50 µm sapphire-based device.

3. Conclusions

In summary, the active-area-dependent performance of PeLEDs under quasi-DC bias, continuous bias, and pulsed bias has been investigated. The EQE_{MAX} and low current density operation of our perovskite architecture are shown not to be affected by excessive Joule heating for all the tested device

areas, both on glass and sapphire substrates, though the performance variation is more significant for the smaller devices. On the contrary, the EQE roll-off behavior and device operational stability under quasi-DC bias and continuous bias are strongly active-area-dependent. We show that scaling down the device size allows to alleviate EQE roll-off and operational instability issues, but not eliminates them. Under pulse-driven operation, the trend of EQE × *J* product of variable-sized devices is similar when suitable pulse patterns are applied, though the smaller devices allow reaching higher current density injection and thus a higher EQE × *J* product value. Using a PeLED with a diameter of 50 μm on the sapphire substrate, we achieve a high quasi-DC radiance of 2059 $W \cdot m^{-2} \cdot sr^{-1}$, half-life time above 10 h under continuous operation at 500 $mA \cdot cm^{-2}$, as well as pulsed EQE × *J* product value of 6.7 $A \cdot cm^{-2}$ at a current density of 4.17 $kA \cdot cm^{-2}$. We note that active area is an important functional parameter that should be discussed when comparing the device performance from different research groups. Moreover, the device downscaling is necessary to decouple the Joule heating from other effects that influence EQE roll-off and device stability. This will help researchers to gain a greater understanding of these effects and eventually find ways to progress towards high brightness applications and, ultimately, perovskite injection lasing.

4. Experimental Section

4.1. Materials. Patterned Glass/ITO (150 nm) substrates with a sheet resistance of 15-20 $\Omega \cdot sq^{-1}$ were purchased from Colorado Concept Coatings. PbI_2 is obtained from TCI Chemicals. Magnesium acetate tetrahydrate, Zinc acetate dihydrate, tetramethylammonium hydroxide (TMAH), ethyl acetate, dimethyl sulfoxide (DMSO), Chlorobenzene, Toluene, and Dimethylformamide (DMF) were purchased from Sigma-Aldrich. Poly-TPD was obtained from 1-Materials. The organic salts for perovskite film preparation were ordered from Greatcell Solar Materials. All the commercial materials were used as received without further purification.

4.2. Substrate preparation. In-house ITO electrodes (150 nm, 30-40 $\Omega \cdot sq^{-1}$) were DC magnetron sputtered through a shadow mask on polished sapphire substrates; glass/ITO substrates were used as received. 125 nm SiN dielectric was deposited on pre-cleaned glass/ITO or sapphire/ITO substrates by means of High-Density Plasma Chemical Vapor Deposition (HDP CVD) at a temperature of 350 °C. Circular features and contact pads were defined with a positive-tone IX845G photoresist that was spin-coated atop SiN at 2000 rpm for 30 sec, baked at 120 °C for 1 min to remove the excess solvent, and exposed by $\lambda \approx 405$ nm light. The exposed features were removed by dipping in OPD5262 developer for 1 min, after which the substrate was rinsed in deionized water (DIW) and dried with compressed N_2. The pattern was transferred to SiN by dry-etching in inductively coupled plasma with SF_6/O_2 gas combination. Finally, the photoresist was removed by ultra-sonification in Microstrip 2001, IPA rinse, and DIW dipping. Shortly before PeLED fabrication, ITO/SiN pixel-defined substrates were cleaned in ultrasonic baths of detergent, DIW, acetone, and IPA successively for 10 minutes in each bath; dried with N_2; and exposed to O_2 plasma (200 W). Additional details are provided in **Supplementary Figure S2**.

4.3. Perovskite film preparation. The details on PMAI-$MAPbI_3$ films' preparation and fabrication were adopted from Rand et al.[18] Perovskite PbI_2 and MAI salts were dissolved together in DMF to obtain a 0.2 M precursor solution. Then, 20 mol% extra benzylammonium iodide was added to form the final $MAPbI_3$:PMAI precursor solution. The perovskite films were fabricated following a typical anti-solvent crystallization process in a N_2 glovebox with the addition of clean dry air. First, perovskite precursor solution was spin-coated at 6000 rpm and then toluene was dropped on the substrates at 3.5 s after commencing spinning. The samples were consequently annealed at 70 °C for 5 min.

ZnMgO nanoparticle synthesis is described in our previous paper.[19] Poly-TPD, PCBM, and ZnMgO were spin-coated at 4000, 3000, and 4000 rpm, respectively. 120 nm Al cathode was evaporated

through a shadow mask with variable width openings, ranging from 500 μm to 2 mm, depending on the device active area. Schematic substrate preparation details and bottom-up device fabrication are presented in **Supplementary Figure S1.**

4.4. Device and film characterization. Radiance-*J*-*V* quasi-DC measurements utilized 20 ms pulses with 20 s idle time to allow for in-between cooling. Continuous DC measurements and quasi-DC measurements were recorded in N_2 glovebox at room temperature with Agilent 4156C Semiconductor Parameter Analyzer, which also synchronously collected the corresponding photodiode current. Thorlabs IS236A-4 integrating sphere coupled with a calibrated SM05PD1B silicon photodiode and a Flame Spectrometer recorded forward-direction electroluminescence intensity and the emission spectrum. The photodiode responsivity together with the integrating sphere were externally pre-calibrated by Thorlabs.

Pulsed sub-μs Radiance-*J*-*V* measurements were done for encapsulated devices in air using an AV-1011-B1-B voltage pulser from Avtech. The absolute current was determined by measuring the voltage drop across a 50 Ω resistor in series with the device. The light signal was collected by a high-speed and large-area SM05PD1B silicon photodetector from Thorlabs. The photodetector signal was then amplified using DHPCA-100 variable gain transimpedance amplifier from FEMTO. The voltage signals and the photodetector signals were synchronously collected using Keithley DSOX3014T oscilloscope. The details of EQE calculation obtained by these methods can be found elsewhere.[34]

All the stability measurements were performed in N_2 glovebox at room temperature and the devices were biased at a constant current density, with light signal recorded in a similar setup to quasi-DC (continuous DC) measurements. In addition, prior to Radiance-*J*–*V* measurements, we applied a continuous current bias of 300-500 $mA \cdot cm^{-2}$ to the devices for 30-60 mins to stabilize their performance.

4.5. Optical and structural measurements. Optical pictures were recorded with a Kiralux 8.9 MP Monochrome Camera from Thorlabs through the glass side in air for encapsulated devices. The electroluminescence signal was collected at a normal incidence. The imaging quality and magnification were carefully calibrated using negative 1951 USAF Test Target from Thorlabs.

Cross-sectional SEM images were obtained from FEI Nova 200 scanning electron microscope, and the SEM specimens were cleaved from the identical silicon-based devices. TEM lamellas were prepared using conventional focused ion beam lift-out carried out on a dual FIB-SEM Helios 450 Nanolab setup by Thermofisher. HR-TEM cross-sectional measurement was performed in a double corrected Titan G2 60-300 manufactured by Thermofisher. HR-TEM image was acquired at 200 kV to ensure high resolution imaging of all the layers.

ASSOCIATED CONTENT

Supporting Information

The following files are available free of charge.

Fabrication details, I-V measurements; obtained statistical EQE distributions; stability measurements, pulsed measurement (PDF).

Conflict of Interest

The authors declare no conflict of interest.

AUTHOR INFORMATION

Corresponding Authors

* Weiming Qiu: E-mail: Weiming.Qiu@imec.be.

* Paul Heremans: E-mail: Paul.Heremans@imec.be.

Author Contributions

The manuscript was written through the contributions of all authors. All authors have given approval to the final version of the manuscript.

ACKNOWLEDGEMENT

The authors acknowledge funding from the European Research Council (ERC) under the European Union's Horizon 2020 research and innovation programme (grant agreement № 835133, ULTRA-LUX). W.Q. would like to thank the financial support of the postdoctoral fellowship grant from FWO.

REFERENCES

(1) Kim, J. Y.; Lee, J. W.; Jung, H. S.; Shin, H.; Park, N. G. High-Efficiency Perovskite Solar Cells. *Chem. Rev.* **2020**, *120* (15), 7867–7918. https://doi.org/10.1021/acs.chemrev.0c00107.

(2) Jeong, M.; Choi, I. W.; Go, E. M.; Cho, Y.; Kim, M.; Lee, B.; Jeong, S.; Jo, Y.; Choi, H. W.; Lee, J.; Bae, J. H.; Kwak, S. K.; Kim, D. S.; Yang, C. Stable Perovskite Solar Cells with Efficiency Exceeding 24.8% and 0.3-V Voltage Loss. *Science (80-.).* **2020**, *369* (6511), 1615–1620. https://doi.org/10.1126/science.abb7167.

(3) Yu, D.; Cao, F.; Gu, Y.; Han, Z.; Liu, J.; Huang, B.; Xu, X.; Zeng, H. Broadband and Sensitive Two-Dimensional Halide Perovskite Photodetector for Full-Spectrum Underwater Optical Communication. *Nano Res.* **2021**, *14* (4), 1210–1217. https://doi.org/10.1007/s12274-020-3174-1.

(4) Fang, Y.; Dong, Q.; Shao, Y.; Yuan, Y.; Huang, J. Highly Narrowband Perovskite Single-Crystal Photodetectors Enabled by Surface-Charge Recombination. *Nat. Photonics* **2015**, *9* (10), 679–686. https://doi.org/10.1038/nphoton.2015.156.

(5) Zou, C.; Chang, C.; Sun, D.; Böhringer, K. F.; Lin, L. Y. Photolithographic Patterning of Perovskite Thin Films for Multicolor Display Applications. *Nano Lett.* **2020**, *20* (5), 3710–3717. https://doi.org/10.1021/acs.nanolett.0c00701.

(6) Gao, Y.; Huang, C.; Hao, C.; Sun, S.; Zhang, L.; Zhang, C.; Duan, Z.; Wang, K.; Jin, Z.; Zhang, N.; Kildishev, A. V.; Qiu, C. W.; Song, Q.; Xiao, S. Lead Halide Perovskite Nanostructures for Dynamic Color Display. *ACS Nano* **2018**, *12* (9), 8847–8854. https://doi.org/10.1021/acsnano.8b02425.

(7) Sutherland, B. R.; Hoogland, S.; Adachi, M. M.; Wong, C. T. O.; Sargent, E. H. Conformal Organohalide Perovskites Enable Lasing on Spherical Resonators. *ACS Nano* **2014**, *8* (10), 10947–10952. https://doi.org/10.1021/nn504856g.

(8) Lei, L.; Dong, Q.; Gundogdu, K.; So, F. Metal Halide Perovskites for Laser Applications. *Adv. Funct. Mater.* **2021**, *2010144*, 1–21. https://doi.org/10.1002/adfm.202010144.

(9) Kim, H.; Kim, J. S.; Heo, J. M.; Pei, M.; Park, I. H.; Liu, Z.; Yun, H. J.; Park, M. H.; Jeong, S. H.; Kim, Y. H.; Park, J. W.; Oveisi, E.; Nagane, S.; Sadhanala, A.; Zhang, L.; Kweon, J. J.; Lee, S. K.; Yang, H.; Jang, H. M.; Friend, R. H.; Loh, K. P.; Nazeeruddin, M. K.; Park, N. G.; Lee, T. W. Proton-Transfer-Induced 3D/2D Hybrid Perovskites Suppress Ion Migration and Reduce Luminance Overshoot. *Nat. Commun.* **2020**, *11* (1), 1–13. https://doi.org/10.1038/s41467-020-17072-0.

(10) Ren, Z.; Li, L.; Yu, J.; Ma, R.; Xiao, X.; Chen, R.; Wang, K.; Sun, X. W.; Yin, W. J.; Choy, W. C. H. Simultaneous Low-Order Phase Suppression and Defect Passivation for Efficient and Stable Blue Light-Emitting Diodes. *ACS Energy Lett.* **2020**, *5* (8), 2569–2579. https://doi.org/10.1021/acsenergylett.0c01015.

(11) Zhao, B.; Bai, S.; Kim, V.; Lamboll, R.; Shivanna, R.; Auras, F.; Richter, J. M.; Yang, L.; Dai, L.; Alsari, M.; She, X. J.; Liang, L.; Zhang, J.; Lilliu, S.; Gao, P.; Snaith, H. J.; Wang, J.; Greenham, N. C.; Friend, R. H.; Di, D. High-Efficiency Perovskite–Polymer Bulk Heterostructure Light-Emitting Diodes. *Nat. Photonics* **2018**, *12* (12), 783–789. https://doi.org/10.1038/s41566-018-0283-4.

(12) Lin, K.; Xing, J.; Quan, L. N.; de Arquer, F. P. G.; Gong, X.; Lu, J.; Xie, L.; Zhao, W.; Zhang, D.; Yan, C.; Li, W.; Liu, X.; Lu, Y.; Kirman, J.; Sargent, E. H.; Xiong, Q.; Wei, Z. Perovskite

Light-Emitting Diodes with External Quantum Efficiency Exceeding 20 per Cent. *Nature* **2018**, *562* (7726), 245–248. https://doi.org/10.1038/s41586-018-0575-3.

(13) Xing, G.; Mathews, N.; Lim, S. S.; Yantara, N.; Liu, X.; Sabba, D.; Grätzel, M.; Mhaisalkar, S.; Sum, T. C. Low-Temperature Solution-Processed Wavelength-Tunable Perovskites for Lasing. *Nat. Mater.* **2014**, *13* (5), 476–480. https://doi.org/10.1038/nmat3911.

(14) Deschler, F.; Price, M.; Pathak, S.; Klintberg, L. E.; Jarausch, D. D.; Higler, R.; Hüttner, S.; Leijtens, T.; Stranks, S. D.; Snaith, H. J.; Atatüre, M.; Phillips, R. T.; Friend, R. H. High Photoluminescence Efficiency and Optically Pumped Lasing in Solution-Processed Mixed Halide Perovskite Semiconductors. *J. Phys. Chem. Lett.* **2014**, *5* (8), 1421–1426. https://doi.org/10.1021/jz5005285.

(15) Pisoni, A.; Jaćimović, J.; Barišić, O. S.; Spina, M.; Gaál, R.; Forró, L.; Horváth, E. Ultra-Low Thermal Conductivity in Organic–Inorganic Hybrid Perovskite CH 3 NH 3 PbI 3. *J. Phys. Chem. Lett.* **2014**, *5* (14), 2488–2492. https://doi.org/10.1021/jz5012109.

(16) Zhao, L.; Roh, K.; Kacmoli, S.; Al Kurdi, K.; Jhulki, S.; Barlow, S.; Marder, S. R.; Gmachl, C.; Rand, B. P. Thermal Management Enables Bright and Stable Perovskite Light-Emitting Diodes. *Adv. Mater.* **2020**, *32* (25), 1–7. https://doi.org/10.1002/adma.202000752.

(17) Zou, C.; Liu, Y.; Ginger, D. S.; Lin, L. Y. Suppressing Efficiency Roll-Off at High Current Densities for Ultra-Bright Green Perovskite Light-Emitting Diodes. *ACS Nano* **2020**, *14* (5), 6076–6086. https://doi.org/10.1021/acsnano.0c01817.

(18) Zhao, L.; Yeh, Y. W.; Tran, N. L.; Wu, F.; Xiao, Z.; Kerner, R. A.; Lin, Y. L.; Scholes, G. D.; Yao, N.; Rand, B. P. In Situ Preparation of Metal Halide Perovskite Nanocrystal Thin Films for

Improved Light-Emitting Devices. *ACS Nano* **2017**, *11* (4), 3957–3964. https://doi.org/10.1021/acsnano.7b00404.

(19) Elkhouly, K.; Goldberg, I.; Boyen, H.-G.; Franquet, A.; Spampinato, V.; Ke, T.-H.; Gehlhaar, R.; Genoe, J.; Hofkens, J.; Heremans, P.; Qiu, W. Operationally Stable Perovskite Light Emitting Diodes with High Radiance. *Adv. Opt. Mater.* **2021**. https://doi.org/10.1002/adom.202100586.

(20) Lee, S. W.; Bae, S.; Hwang, J. K.; Lee, W.; Lee, S.; Hyun, J. Y.; Cho, K.; Kim, S.; Heinz, F. D.; Bin Choi, S.; Choi, D.; Kang, D.; Yang, J.; Jeong, S.; Park, S. J.; Schubert, M. C.; Glunz, S.; Kim, W. M.; Kang, Y.; Lee, H. S.; Kim, D. Perovskites Fabricated on Textured Silicon Surfaces for Tandem Solar Cells. *Commun. Chem.* **2020**, *3* (1), 1–11. https://doi.org/10.1038/s42004-020-0283-4.

(21) Han, Q.; Hsieh, Y. T.; Meng, L.; Wu, J. L.; Sun, P.; Yao, E. P.; Chang, S. Y.; Bae, S. H.; Kato, T.; Bermudez, V.; Yang, Y. High-Performance Perovskite/ Cu(In,Ga)Se2 Monolithic Tandem Solar Cells. *Science (80-.).* **2018**, *361* (6405), 904–908. https://doi.org/10.1126/science.aat5055.

(22) Elkhouly, K.; Gehlhaar, R.; Genoe, J.; Heremans, P.; Qiu, W. Perovskite Light Emitting Diode Characteristics: The Effects of Electroluminescence Transient and Hysteresis. *Adv. Opt. Mater.* **2020**, *8* (23), 1–8. https://doi.org/10.1002/adom.202000941.

(23) Yoshida, K.; Nakanotani, H.; Adachi, C. Effect of Joule Heating on Transient Current and Electroluminescence in P-i-n Organic Light-Emitting Diodes under Pulsed Voltage Operation. *Org. Electron.* **2016**, *31*, 287–294. https://doi.org/10.1016/j.orgel.2016.01.039.

(24) Cao, Y.; Wang, N.; Tian, H.; Guo, J.; Wei, Y.; Chen, H.; Miao, Y.; Zou, W.; Pan, K.; He, Y.; Cao, H.; Ke, Y.; Xu, M.; Wang, Y.; Yang, M.; Du, K.; Fu, Z.; Kong, D.; Dai, D.; Jin, Y.; Li, G.; Li, H.; Peng, Q.; Wang, J.; Huang, W. Perovskite Light-Emitting Diodes Based on Spontaneously Formed Submicrometre-Scale Structures. *Nature* **2018**, *562* (7726), 249–253. https://doi.org/10.1038/s41586-018-0576-2.

(25) Karlsson, M.; Yi, Z.; Reichert, S.; Luo, X.; Lin, W.; Zhang, Z.; Bao, C.; Zhang, R.; Bai, S.; Zheng, G.; Teng, P.; Duan, L.; Lu, Y.; Zheng, K.; Pullerits, T.; Deibel, C.; Xu, W.; Friend, R.; Gao, F. Mixed Halide Perovskites for Spectrally Stable and High-Efficiency Blue Light-Emitting Diodes. *Nat. Commun.* **2021**, *12* (1), 1–10. https://doi.org/10.1038/s41467-020-20582-6.

(26) Fakharuddin, A.; Qiu, W.; Croes, G.; Devižis, A.; Gegevičius, R.; Vakhnin, A.; Rolin, C.; Genoe, J.; Gehlhaar, R.; Kadashchuk, A.; Gulbinas, V.; Heremans, P. Reduced Efficiency Roll-Off and Improved Stability of Mixed 2D/3D Perovskite Light Emitting Diodes by Balancing Charge Injection. *Adv. Funct. Mater.* **2019**, *29* (37), 1–12. https://doi.org/10.1002/adfm.201904101.

(27) Xu, W.; Hu, Q.; Bai, S.; Bao, C.; Miao, Y.; Yuan, Z.; Borzda, T.; Barker, A. J.; Tyukalova, E.; Hu, Z.; Kawecki, M.; Wang, H.; Yan, Z.; Liu, X.; Shi, X.; Uvdal, K.; Fahlman, M.; Zhang, W.; Duchamp, M.; Liu, J. M.; Petrozza, A.; Wang, J.; Liu, L. M.; Huang, W.; Gao, F. Rational Molecular Passivation for High-Performance Perovskite Light-Emitting Diodes. *Nat. Photonics* **2019**, *13* (6), 418–424. https://doi.org/10.1038/s41566-019-0390-x.

(28) Cho, H.; Kim, Y. H.; Wolf, C.; Lee, H. D.; Lee, T. W. Improving the Stability of Metal Halide Perovskite Materials and Light-Emitting Diodes. *Adv. Mater.* **2018**, *30* (42), 1–24.

https://doi.org/10.1002/adma.201704587.

(29) Yuan, Y.; Wang, Q.; Shao, Y.; Lu, H.; Li, T.; Gruverman, A.; Huang, J. Electric-Field-Driven Reversible Conversion between Methylammonium Lead Triiodide Perovskites and Lead Iodide at Elevated Temperatures. *Adv. Energy Mater.* **2016**, *6* (2), 1–7. https://doi.org/10.1002/aenm.201501803.

(30) Dong, Q.; Lei, L.; Mendes, J.; So, F. Operational Stability of Perovskite Light Emitting Diodes. *J. Phys. Mater.* **2020**, *3* (1), 012002. https://doi.org/10.1088/2515-7639/ab60c4.

(31) Huang, Z.; Proppe, A. H.; Tan, H.; Saidaminov, M. I.; Tan, F.; Mei, A.; Tan, C. S.; Wei, M.; Hou, Y.; Han, H.; Kelley, S. O.; Sargent, E. H. Suppressed Ion Migration in Reduced-Dimensional Perovskites Improves Operating Stability. *ACS Energy Lett.* **2019**, *4* (7), 1521–1527. https://doi.org/10.1021/acsenergylett.9b00892.

(32) Kim, H.; Zhao, L.; Price, J. S.; Grede, A. J.; Roh, K.; Brigeman, A. N.; Lopez, M.; Rand, B. P.; Giebink, N. C. Hybrid Perovskite Light Emitting Diodes under Intense Electrical Excitation. *Nat. Commun.* **2018**, *9* (1), 4893. https://doi.org/10.1038/s41467-018-07383-8.

(33) Qin, J.; Liu, X. K.; Yin, C.; Gao, F. Carrier Dynamics and Evaluation of Lasing Actions in Halide Perovskites. *Trends in Chemistry*. The Author(s) 2021, pp 34–46. https://doi.org/10.1016/j.trechm.2020.10.010.

(34) Yan, J.; Croes, G.; Fakharuddin, A.; Song, W.; Heremans, P.; Chen, H.; Qiu, W. Exploiting Two-Step Processed Mixed 2D/3D Perovskites for Bright Green Light Emitting Diodes. *Adv. Opt. Mater.* **2019**, *7* (15), 3–11. https://doi.org/10.1002/adom.201900465.